



Real-time monitoring of biomechanical activity in aphids by laser speckle contrast imaging

STOYAN YORDANOV,^{1,3} MARTIN DRUCKER,^{2,4} HANS-JÜRGEN BUTT,¹ AND KALOIAN KOYNOV¹

¹Max Planck Institute for Polymer Research, Ackermannweg 10, D-55128 Mainz, Germany

²INRAE – French National Research Institute for Agriculture, Food and Environment, UMR 1131 SVQV, 28 Rue de Herrlisheim, 68000 Colmar, Université de Strasbourg, France

³yordanov.stoyan@gmail.com

⁴martin.drucker@inrae.fr

Abstract: Studying *in vivo* feeding and other behaviors of small insects, such as aphids, is important for understanding their lifecycle and interaction with the environment. In this regard, the EPG (electrical penetration graph) technique is widely used to study the feeding activity in aphids. However, it is restricted to recording feeding of single insects and requires wiring insects to an electrode, impeding free movement. Hence, easy and straightforward collective observations, e.g. of groups of aphids on a plant, or probing other aphid activities in various body parts, is not possible. To circumvent these drawbacks, we developed a method based on an optical technique called laser speckle contrast imaging (LSCI). It has the potential for direct, non-invasive and contactless monitoring of a broad range of internal and external activities such as feeding, hemolymph cycling and muscle contractions in aphids or other insects. The method uses a camera and coherent light illumination of the sample. The camera records the laser speckle dynamics due to the scattering and interference of light caused by moving scatters in a probed region of the insect. Analyzing the speckle contrast allowed us to monitor and extract the activity information during aphid feeding on leaves or on artificial medium containing tracer particles. We present evidence that the observed speckle dynamics might be caused by muscle contractions, movement of hemocytes in the circulatory system or food flows in the stylets. This is the first time such a remote sensing method has been applied for optical mapping of the biomechanical activities in aphids.

© 2021 Optical Society of America under the terms of the [OSA Open Access Publishing Agreement](#)

1. Introduction

Aphids and other piercing-sucking arthropods are important pests in agriculture. This is due to their high multiplication rates on infested plants and their feeding behavior. Aphids are specialized on feeding from the sap of the phloem, the plants' equivalent of animal circulatory system. The phloem sap contains high levels of sugars and low levels of amino acids. This imbalance forces the insects to ingest great quantities of sap to ensure sufficient supply of amino acids and to excrete excess sugars in the form of honeydew.

Aphids have a particular feeding behavior [1–3]. When alighting on a plant, they first insert their stylets (the aphids' needle-like mouthparts containing a salivary and a food canal that merge to form a common canal at the stylet tips into the epidermis and mesophyll. While moving in these tissues, the stylets puncture individual cells to taste the plants. The exploratory punctures consist of a brief phase of injection of saliva into the cells, followed by active ingestion of some cell contents. If the aphids accept the plant, the punctures continue in other cells until the stylets reach the phloem vessels. Here the feeding behavior changes. An initial salivation event is followed by a prolonged (hours and more) feeding phase consisting of ingestion of phloem sap interspersed with short salivation phases. Phloem feeding is passive and driven by the high hydrostatic pressure in the phloem that forces the phloem sap through the stylets into the aphids'

digestive system. Aphids counteract the high pressure supposedly by opening and closing the cibarial valve, located between the stylets and the intestine, and thus control the flow rate in the stylets.

Aphids cause damage trifold [4]. Removal of phloem sap weakens plants and the honeydew deposited on the leaves attracts fungi, causing indirect damage. Finally, aphids are important virus vectors that as “flying syringes” acquire and inoculate viruses with great precision directly from and into cells and phloem vessels. Studying aphid feeding behavior is therefore of special interest. The introduction of the Electrical Penetration Graph (EPG) technology together with microscopic analysis helped tremendously to uncover the different feeding behaviors [2]. However, the physics of aphid feeding is still largely unknown. For example, only few data on flow rates in the stylets are available. Rough estimates of active and passive ingestion rates were obtained from aphids feeding on radioactively labeled medium from sachets, quantification of honeydew excretions and phloem exudates from dissected stylets. Results vary greatly (for resume [5]). Even less is known about reversal of flows during feeding activity, although it is clear that it occurs to allow switching between salivation (outward flow), ingestion (inward flow), and the less characterized egestion.

A similar challenge is faced when attempting to measure flow of hemolymph (insect blood). Most methods are complicated or expensive. For example, dynamic x-ray phase-contrast imaging can be used to record hemolymph movement even in the interior of insects such as in the heart of a grasshopper [6]. Fluorescence-based methods are easier to apply and have been used to visualize, for example, hemolymph flow in the auxiliary heart in the wing of a mosquito [7]. However, these methods remain limited to measurements close to the surface of the insect body. In addition, both methods depend on the injection of tracer molecules to visualize flows. To our knowledge, no data are available for hemolymph movement in aphids measured with or without tracers.

Therefore, new non-invasive methods are needed to study aphids or other small insects, for example, to measure flow rates in their stylets or to monitor other physiological parameters such as hemolymph flow. Note that the technique of choice must be able to probe regions below the highly scattering and opaque surface of the stylets and the labium (see Fig. 3 for stylet anatomy).

Laser speckle contrast imaging (LSCI) is an optical technique that measures the laser speckle contrast by imaging the temporal and spatial fluctuations of laser speckle pattern due to movements of scatters in a sample volume. A camera is employed to capture series of frames of an object under coherent light illumination (e.g. from laser). From the recorded frames, LSCI estimates the contrast by exploiting the statistical properties of the recorded laser speckle pattern. The speckle pattern manifests itself as small grainy structure imprinted in the object captured on a 2D image. The grainy structure is caused by the interference of multiple coherent light fields coming from different scatters in the sample. Any movement of scatters causes changes in the optical beam paths of the interfering rays and this in turn changes the phases of the scattering light fields that interfere, and hence the observed local intensity fluctuates in space and time. These spatial and/or temporal intensity variations carry information (via the speckle contrast) about the dynamics of the underlying process, such as diffusion, flow or other types of motion [8–11]. Thus, LSCI (single light scattering regime) or DWS (diffuse wave spectroscopy, i.e. multiple light scattering regime) have the ability to probe processes on the surface, near the surface as well as deeper in the tissue, i.e. below the surface of a species [9,12,13]. To date LSCI technique is mainly used in biomedical applications, for example, to measure tissue perfusion, skin perfusion, cerebral blood flow, retinal blood flow and brain activity in humans or small animals [9,14–16].

Here, we explore the feasibility of LSCI to monitor various processes and events in aphids. We mapped the activity in an aphid and in a group of aphids, likely due to hemolymph movement (circulating hemocytes) or muscle movements and we measured flow velocity in the stylets. We show that the underlying speckle dynamics can be observed directly, i.e. monitoring aphids

without the use of tracers is possible. However, for the feeding flow velocity measurements in the stylet we used 100 nm non-labeled PS (polystyrene) nanoparticles to increase the scattering signal and thus facilitate the detection of the corresponding flow.

2. Materials and methods

2.1. Experimental LSCI microscopy setup

The experimental setup, Fig. 1(a), consists of highly coherent illumination source (He-Ne laser, 5 mW optical power, 633 nm wavelength) fiber coupled to a standard Single Mode Fiber (SMF) with numerical aperture $NA = 0.15$. After out-coupling, the light is collimated by a collimator lens CL (achromatic doublet, $f = 30 \text{ mm}$) to ca. 10 mm beam diameter and passes subsequently through half wave plate ($\text{HWP or } \lambda/2$), linear polarizer LP1 and lens L1 (singlet, $f = 300 \text{ mm}$). The role of the HWP and the LP1 subsystem is to control the illumination power by fixing the polarization plane (by LP1) and adjusting the incoming light polarization by rotating HWP. Note that using SMF is not mandatory but facilitates light delivery and control. The L1 lens ($f = 300 \text{ mm}$) introduces divergence or convergence of the light and thus controls the size of the illuminated area on the sample.

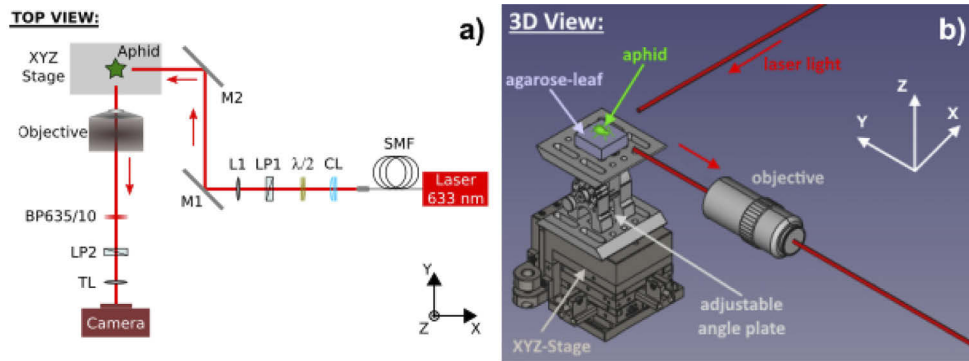


Fig. 1. Experimental LSCI microscopy setup. (a) A scheme of the experimental setup (SMF – Single Mode Fiber, CL – Collimator, $\lambda/2$ – Half Wave Plate, LP1/LP2 – Linear Polarizers, L1 – Lens, TL – Tube Lens, M1/M2 – Mirrors, BP635/10–635 \pm 5 nm Bandpass Filter); (b) 3D view of the setup (showing the geometry of the illumination and sample) – the aphid is positioned on a leaf mounted on top of an agarose slab in a Petri dish, which is mounted on an adjustable angle plate (AP180, Thorlabs) and manual XYZ stage (562-XYZ, Newport) to position the sample, the objective is Mitutoyo 10x/0.28NA Plan Apo HR LD (Edmund optics); the red arrows indicate the direction of light propagation and collection; the aphid in (a) is symbolized by the green star.

The scattered signal from the aphid was detected by a 10x/0.28NA Mitutoyo objective (Plan Apo Infinity Corrected Long Working Distance Objective) having a focal length of 20 mm used with tube lens TL of $f = 100 \text{ mm}$ focal length delivering 5x magnification. The point spread function (PSF) diameter for this objective at 633 nm wavelength is $d_{\text{PSF}} = 2.76 \mu\text{m}$, and hence the maximum resolution achievable is $r_{\text{PSF}} = d_{\text{PSF}}/2 = 1.38 \mu\text{m}$. However, we sampled only half of it, i.e. the camera pixel size equals the resolution in the objective space in order to keep the field of view (FOV) big enough to fit an entire aphid on the image sensor. Also, for LSCI imaging, the pixel size is acceptable to be as big as the resolution to properly sample the laser speckle whose minimum size cannot be smaller than the size of the PSF. Thus, we satisfy the Nyquist criterion that the optimal number of camera pixels to sample a laser speckle is 2 or higher. After the objective, the signal was relayed to an optical bandpass filter BP635/10 (635 \pm 5 nm),

which filters the ambient light and allows only the useful signal at 633 nm wavelength to pass through. The next element, the linear polarizer LP2, acts as additional selective element for the polarization of the detected scattered light – if it is colinear with the illumination polarization it will detect more of the signal from the surface, while if it is in orthogonal plane it will reduce the specular reflection and probe deeper in the sample. Finally, the tube lens TL images the observed sample on a camera (DMK 33UX287, The Imaging Source GmbH): 720×540 pixels, $6.9 \times 6.9 \mu\text{m}^2$ pixel size, USB3, monochrome, 12-bit dynamic range, up to 539 fps (8 bit), exposure time from 1 μs up to 30 s. When we wanted to observe a bigger field of view, we removed the microscope objective and observed the scene only with the TL in front of the camera. Thus, the TL in this case acted as a simple photographic objective, which in our case resulted in image magnification of 0.4x on the camera. This resulted in under sampling of the laser speckle by factor of 1.6. Such under sampling would cause additional loss in contrast due to additional spatial averaging at the detector side (failure to satisfy Nyquist criterion). Note that using the TL alone as a camera objective for imaging will require refocusing since the object is at finite distance from the tube lens, i.e. not in the infinity space of the objective.

We used red light in our experiments because aphids are insensitive to this spectral region or above [17]. This allows the red light to be used as a probe that does not cause any irritation or other side effects in the aphid's behavior. In addition, regarding the VIS (Visible) range, the red light penetrates deeper in the tissue so that it is better suited to probe underneath the surface than shorter wavelengths.

2.2. LSCI theory

LSCI tracks the dynamic changes in a 2D speckle pattern by measuring the so called laser speckle contrast K of the scattered light and if a model is available it can relate it to a physical parameter(s) of the underlying process (e.g. flow or diffusion). The speckle contrast K is defined as the ratio of the standard deviation σ of the intensity over the mean intensity I in the spatial or/and temporal domain:

$$K = \frac{\sigma}{\langle I \rangle} \quad (1)$$

The contrast K is a time average quantity, which depends on the exposure time T . For example, in the spatial domain, if there is no change in speckle intensity for a given time period (e.g. no movements of scatters), $K = 1$, i.e. maximal contrast. On the other hand, if there are movements of scatters, the contrast decreases due to local speckle intensity pattern decorrelation, i.e. blurring. In the ultimate case when the velocity of the scatters is infinite for given integration time, the contrast $K = 0$. Mathematically, the speckle contrast K is expressed as a function of the time average, for given time exposure T , of the auto-covariance of the intensity fluctuations $C_t(\tau)$ in a given laser speckle [9,18]:

$$K^2(T) = \frac{2}{T\langle I \rangle^2} \int_0^T \left(1 - \frac{\tau}{T}\right) C_t(\tau) d\tau = \frac{2\beta}{T} \int_0^T \left(1 - \frac{\tau}{T}\right) |g_1(\tau)|^2 d\tau \quad (2)$$

In the latter we used the fact that the auto-covariance is related to the electric field auto-correlation through $C_t(\tau) = \beta I_t^2 |g_1(\tau)|^2$, where β is a coefficient that accounts for reduction in contrast due to the ratio of the pixel to speckle size, depolarization effects and noise. This formulation of K allows to use auto-correlation functions $g_1(\tau)$ from DLS (dynamic light scattering) theory. In our case, we assumed $g_1(\tau) = \exp(-\tau/\tau_c)$, which describes either single light scattering regime and diffusion (unordered motion) or multiple scattering and directed flow (ordered motion). For extended list of different $g_1(\tau)$ used in LSCI, see [Supplement 1](#), Table S1.

Thus, K is implicitly dependent on the (de-)correlation time τ_c of the auto-covariance $C_t(\tau)$ of the speckle intensity fluctuations. The correlation time τ_c is the time period after which the speckle pattern is decorrelated, i.e. changes significantly. Therefore, the longer the exposure

time the higher the decorrelation and lower the contrast. The faster the underlying process, the shorter the τ_c is, and vice versa.

There are number of analytical and approximation expressions in literature that relate contrast K and the correlation time τ_c . Here we will present only the ones relevant to this article. So, after calculating the contrast K from the raw speckle, which is straightforward, the next step in the data analysis is to find out τ_c . Using the el. field auto-correlation above, i.e. $g_1(\tau) = \exp(-\tau/\tau_c)$, it is possible to derive analytically the respective relationship of K and τ_c [18–20]:

$$K(T, \tau_c) = \left\{ \beta \frac{\exp(-2x) - 1 + 2x}{2(x)^2} \right\}^{\frac{1}{2}} \quad (3)$$

where $x = T/\tau_c$. Hence, fixing exposure time T and calculating K allows to numerically extract (β can be estimated by a calibration measurement). However, there is often static scattering and noise in a real experiment, therefore a more rigorous form of Eq. (3) was derived that accounts for these effects [9,21,22]:

$$K(T, \tau_c) = \left\{ \beta \rho^2 \frac{\exp(-2x) - 1 + 2x}{2x^2} + 4\beta\rho(1-\rho) \frac{\exp(-x) - 1 + x}{x^2} + \beta(1-\rho)^2 \right\}^{\frac{1}{2}} + C_{noise} \quad (4)$$

where $\rho = I_f/(I_f + I_s)$ is the fraction of the dynamically scattered light; I_f – the intensity of the dynamically scattered light, I_s – the intensity of the statically scattered light. The term C_{noise} accounts for the experimental background noise and can be interpreted as the offset of the base speckle contrast due to presence of noise. This equation for the contrast K is used in the so called MESI method (multi-exposure speckle imaging), i.e. by measuring K for different exposure times T it allows to precisely determine τ_c , β , ρ , C_{noise} from the fit of the $K(T, \tau_c)$ vs T curve. We used this approach for flow velocity estimation in the stylets of the aphid.

The disadvantage of Eqs. (3) and (4) is that they are computationally very intensive to calculate. Therefore, we used them only for point like measurements or estimating K over ROI, i.e. fitting single $K(T, \tau_c)$ vs T curve. For all other activity measurements in 2D we used the following approximation to extract τ_c [23]:

$$\frac{1}{\tau_c} = \frac{1}{TK^2} \quad (5)$$

This approximation is valid for $T \geq 2\tau_c$, i.e. $0 < K < 0.6$.

A more direct way to extract the auto-covariance $C_t(\tau)$ and τ_c from the temporal intensity fluctuations $I(t)$ of the laser speckle was proposed [24]. The method is called FDLSI (frequency domain laser speckle imaging) and we also evaluated it for flow velocity estimation in the stylet of the aphid. However, this method is also computationally intensive. In addition, the exposure time must correspond to the frame rate of the camera to sample properly the intensity time trace. However, this limits the time resolution with respect to τ_c to the inverse of the maximum frame rate. Computing the respective $C_t(\tau)$ is done by [24]:

$$C_t(\tau) = \int_{-\infty}^{\infty} PSD(\omega) e^{i\omega\tau} d\omega - I^2 \quad (6)$$

where the power spectral density is equal to $PSD(\omega) = |\tilde{I}(\omega)|^2 = |\mathcal{F}\{I(t)\}|^2$, i.e. PSD is the square amplitude of the Fourier transform of the input intensity signal $I(t)$ in the time domain. The authors derived two different functions for fitting the auto-covariance $C_t(\tau)$ and extracting the correlation time τ_c . The first function was derived to account for particles motion having

uniform velocity [24]:

$$C_t(\tau) = \exp\left(-\frac{\tau^2}{\tau_c^2}\right) \quad (7)$$

The second function was derived to account for particles motion resulting from unordered (Brownian) motion and highly ordered motion with Gaussian distribution of the velocities [24]:

$$C_t(\tau) = \exp\left(-\frac{V_f^2 \tau^2}{l_c^2 + V_d^2 \tau^2}\right) \left\{ \frac{l_c^3}{(l_c^2 + V_d^2 \tau^2)^{\frac{3}{2}}} + \frac{2V_f^2 V_d^2 l_c \tau^4}{(l_c^2 + V_d^2 \tau^2)^{\frac{5}{2}}} \right\} \quad (8)$$

where l_c is the so called (de-)correlation length, V_f is the mean velocity of the ordered motion (directed flow) and V_d is the root mean square velocity due to the unordered motion (Brownian diffusion). Fitting $C_t(\tau)$ with this equation allows to estimate the V_f and V_d with respect to this model.

After extracting the correlation time τ_c , by fitting $K(T, \tau_c)$ or $C_t(\tau)$ curves, or simply by single exposure LSCI measurement, we can evaluate the activity of the system in terms of velocity (Brownian motion or directed flow). We used the velocity V as defined in [24]:

$$V = \frac{l_c}{\tau_c} \quad (9)$$

There, the (de-)correlation length l_c is defined as the distance where the overlap of two Airy discs equals $1/e$ of the original area [24]:

$$l_c = 0.67 r_{\text{Airy}} = 0.41 \frac{\lambda}{NA} \quad (10)$$

where λ is the wavelength of the illumination light, NA is the numerical aperture of the imaging system and $r_{\text{Airy}} = 1.22\lambda/2NA$ is the radius of the Airy disk. In our data analysis we used this definition of (de-)correlation length l_c when calculating the corresponding velocity for the different LSCI analysis methods. More elaborated presentation of the LSCI theory can be found in “Supplement 1, S1: LSCI theory”.

2.3. LSCI data processing

LASCA (laser speckle contrast analysis) is used to convert the raw speckle images to contrast maps, then to correlation time maps and subsequently to velocity maps (used as activity indicator). Here we define the activity as every process (external or internal) in the aphids that causes dynamic changes in the laser speckle and can thus be monitored by this technique. From LSCI point of view, one can use few estimators of the activity – contrast K , correlation time τ_c and velocity V . The former two are pure statistical estimators and not directly related to a physical quantity. For example, τ_c is the decaying rate of $C_t(\tau)$ and shows how fast speckle changes. Contrast K is dependent on exposure time, therefore, it is not invariant with respect to the choice of experimental settings. Thus, we decided to characterize the activity in terms of a physical quantity – namely, we used velocity as activity indicator. Bear in mind that if the underlying physical process is unknown, the interpretation of velocity might mean nothing more than how fast speckle changes due to unknown process causing scatters or scattering structures to move.

The main methods that we used to acquire and process the raw data were sLASCA (spatial LASCA) [9], sMESI (single exposure multi-exposure speckle imaging) [25] and FDLSI (frequency domain laser speckle imaging) [24]. A schematic drawing of how these methods work is shown on Fig. 2. A more detailed description of these methods can be found in “Supplement 1, S2: LSCI data processing” section.

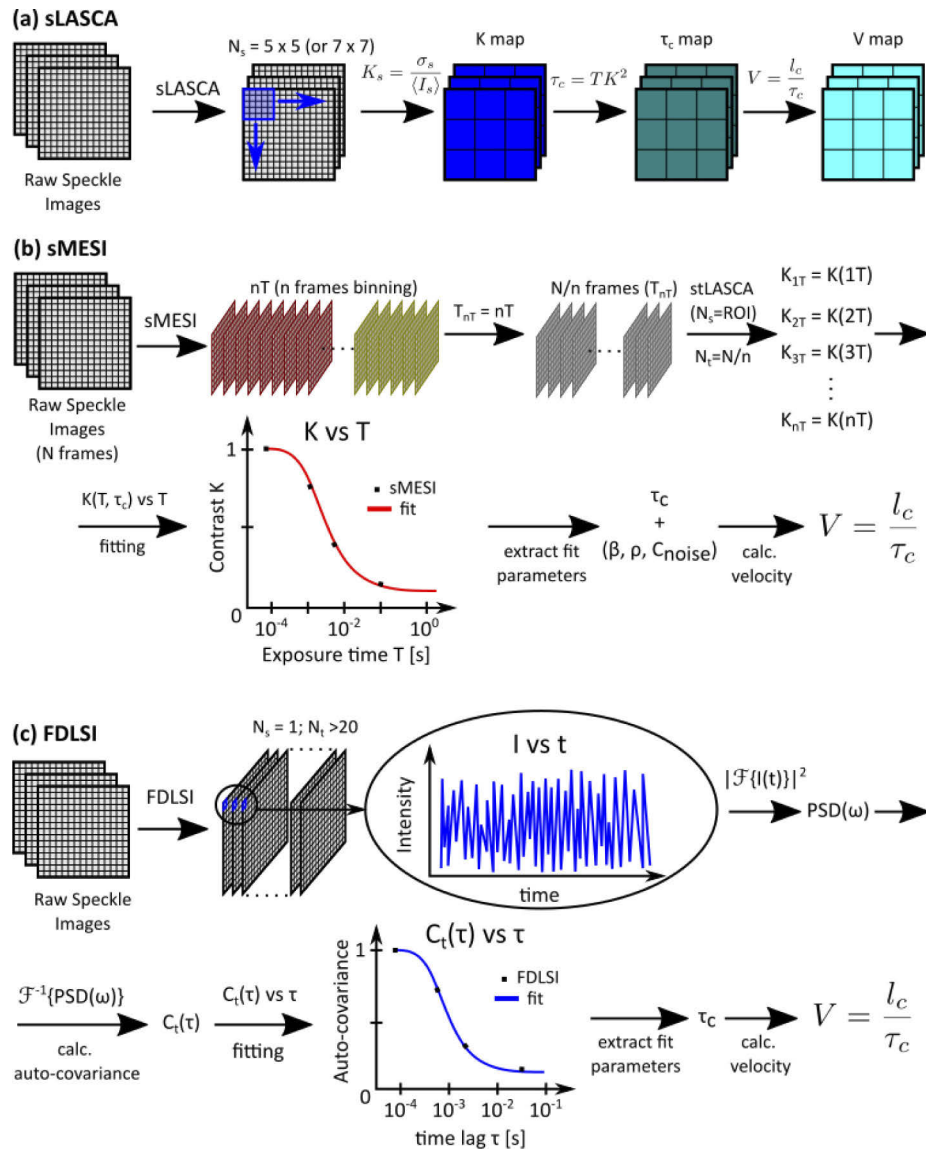


Fig. 2. The main LASCA methods used in the data processing. (a) sLASCA converts the raw speckle images into contrast K map, correlation τ_c map and velocity V map using the spatial speckle fluctuations. There is a loss of spatial resolution due to how K is calculated; (b) sMESI records sequence of frames with single exposure and then builds multi-exposure frames processed with stLASCA (Spatio-Temporal LASCA) to extract contrast $K(T)$ vs T curve for a given ROI. Fitting this curve with suitable model yields τ_c , β , C_{noise} and subsequently the velocity V ; (c) FDLSI uses the fluctuations in the intensity in the temporal direction (I vs t) to calculate the PSD ($|\mathcal{F}\{I(t)\}|^2$). Subsequently the auto-covariance $C_t(\tau)$ is calculated as the inverse Fourier Transform of PSD. Fitting this curve with a model yields τ_c and subsequently V . N_s – the size of the spatial sliding window, N_t – the size of the temporal window. See “Supplement 1, S2: LSCI data processing” section for in depth description.

The data processing and workflow procedure was according to the following main steps: (a) a raw video was recorded either in 8 bit or 16 bit (actual 12-bit dynamic range) format; (b) each raw recorded video was converted to a multipage tiff file for easy examination and further processing; (c) one or more of the above speckle analysis methods were used to estimate the speckle contrast and subsequently the velocity.

The sLASCA method was used to calculate 2D maps of the velocity (activity). For the flow velocity estimation in the stylets, sMESI and FDLSI were used as they give a more accurate estimation of the velocity due to corrections for static scattering and noise. Most of the time we used camera frame rates set near the maximum possible, i.e. 500 fps (2 ms exposure time), and acquired 1000 frames per experiment. For the long time scale LSCI experiments we used 1 fps to reduce the amount of data to be stored. For acquiring the raw laser speckle images, we used the software provided with the camera (IC Capture v2.4, The Imaging Source). The data processing algorithms were implemented in MATLAB and the code as used in this article is freely available [26].

2.4. Aphids and plants

The green peach aphid (*Myzus persicae* (Sulzer)) colony originated from a clone isolated in the Netherlands. Wingless aphids were reared in insect-proof cages on Chinese cabbage (*Brassica rapa pekinensis var. Granaat*) in a growth chamber under controlled conditions (60% humidity, a temperature of $20 \pm 1^\circ\text{C}$ and a photoperiod of 16 h day / 8 h night). Aphids were transferred to new host plants when populations were crowded but before appearance of winged aphids (see Fig. 3).

The typical size of the food canal is about 1 μm in diameter and several hundred microns long. The aphid intestine (stomach, midgut, hindgut, rectum) is about 4 mm long, its diameter ranges from 40-150 μm (200 μm for the stomach).

Turnip plants (*Brassica rapa rapa var. Just Right*) were sown in Humin-Substrat N2, pH 5.8 (Neuhaus, Geeste, Germany) and grown under controlled conditions (60% humidity, a temperature of $20 \pm 1^\circ\text{C}$ and a photoperiod of 14 h day / 10 h night).

2.5. Aphid manipulation

Wingless adult aphids were manipulated with a small brush. To observe aphids on leaves, 1% (w/v) molecular biology grade agarose (Euromedex) in water was melted and poured in a Petri dish. When the agarose had cooled down and started to solidify ($\sim 37^\circ\text{C}$), a leaf of 3-5 cm length was detached from a turnip plant, cut in traverse direction and the lower half of the leaf was placed upside down on the agarose. Once the agarose had polymerized, one or more aphids were transferred to the leaf and it was used for the experiments. This set-up provided a leaf surface amenable for microscopy, which could be used for long observations (hours to days) because the agarose stabilized the leaf mechanically and prevented desiccation.

For observation of non-feeding aphids, individuals were immobilized on the stage by placing them carefully on a double-faced adhesive tape. This setup impeded aphid movement and allowed observation for several hours.

For observation of aphids feeding from artificial medium, a Parafilm membrane (Sigma) was stretched over the rim of a 35 mm Petri dish and 100-200 μl feeding solution (10% sucrose, containing or not nanoparticles) were deposited on the surface of the Parafilm. Then a second, maximally stretched Parafilm membrane was placed on the first membrane to enclose the feeding solution and form a sachet. The sachet together with its Petri dish support were fixed on the stage and aphids were placed on the membrane for feeding.

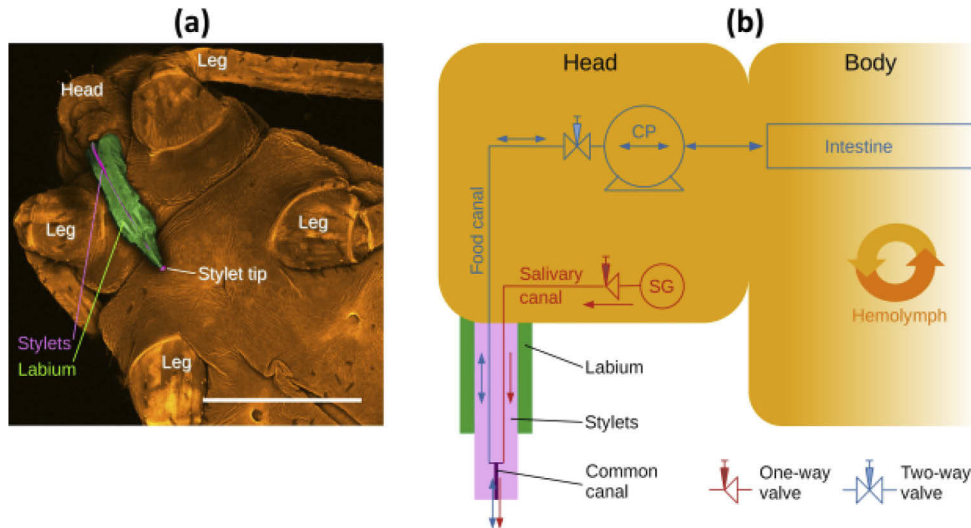


Fig. 3. Food, saliva and hemolymph flows in aphids. (a) Image of an aphid (in autofluorescence) - reconstructed from a maximum intensity projection of a 3D stack acquired with Zeiss LSM510 confocal laser scanning unit using 10x/0.3NA objective and 488 nm laser excitation (fluorescence signal collected with LP505 filter). Presented is a ventral view of the aphid body (orange) showing the upper parts of four of the six legs and the lower part of the head. The stylets (pink) form a tube-like structure. They exit from the head and are contained in the middle cleft of the labium (green) that protects and guides the stylets. The stylet tip containing the common canal is visible at the lower end of the labium. The stylets in this picture are retracted and in standby position; when aphids are feeding they extrude for several hundred μm and penetrate deep into the plant tissue. Scale bar: 500 μm ; (b) Diagram of food (blue), saliva (red) and hemolymph (orange) flows in aphids. Saliva is produced in the salivary glands (SG) and secreted into the salivary canal. The salivary canal passes from the salivary glands through the head and the stylets. It merges with the food canal at the stylet tips to form the common canal (purple). Food enters into the stylets through the common canal and then finds its way through the food canal to the cibarial pump (CP) and further into the intestine. The cibarial pump as a peristaltic pump is bidirectional and controls the flow direction and speed of fluids in the food canal. This is symbolized by the pump and valve pictogram. This allows for inward-directed food ingestion and outward-directed egestion. The flow in the saliva canal is unidirectional and permits only outward-directed salivation. Hemolymph is pumped through a dorsal tube-like heart that is open at its two ends (not shown). This creates a rather slow circular stream, which is presented by the circular arrows.

2.6. Nanoparticle tracers

For the flow velocity experiment in the stylets we used 100 nm diameter, unlabeled (no fluorescence), polystyrene nanoparticles as tracers to enhance the scattering signal. The nanoparticles were purchased from Kisker-Biotec GmbH, Germany (PPS-0.1/plain/0.1 μm /15 mL/2.5%).

3. Results

3.1. Group of aphids feeding on a leaf – feeding experiments with low resolution LSCI

In the first experiment we observed the feeding behavior of a group of aphids. An overview bright-field image of the aphids is shown in Fig. 4(a). The aphids were positioned on a leaf so that we could monitor their natural feeding behavior. We distinguished between the following feeding behaviors: pre-feeding as the behavior of a resting aphid freshly placed on a leaf that did not yet feed on the phloem; it takes on average about one hour for an aphid to reach the phloem. Feeding is defined as the behavior of a non-moving aphid that had been on the leaf for more than one hour and thus probably reached the phloem. After-feeding is the behavior when the aphid is not feeding anymore – the aphid is removed from the leaf and immobilized on adhesive tape, without access to a food source. No tracer particles were used to enhance the laser scattering. The observed speckle originated from the light scattering due to internal and/or external aphid's activity (movements, flow etc.). In the Supplement a video of the feeding aphids is available (see [Visualization 1](#)) showing the corresponding laser speckle patterns dynamically changing due to the aphids' internal body activity.

After the aphids settled on a given location we illuminated them with 633 nm laser light and recorded their activity by LSCI microscopy (Fig. 5). The objective was unmounted, and the tube lens played the role of a camera objective. We monitored the long and short time scales activities and thus captured events on the corresponding time scales – 1 s and 2 ms, respectively. The mean intensity map, Fig. 5(a) and Fig. 5(d), shows the smoothing effect on the aphid bodies since due to their activity the 2D intensity speckle pattern fluctuates in space and time and after averaging over many frames the speckle structure blurs. On the other hand, in areas where there were no movements of scatterers, the speckle pattern was static, and the surrounding surface area kept its grainy structure (indicating static speckle). This smoothing effect, due to dynamically changing speckle pattern, is quantitatively related to the contrast – the higher the smoothness the smaller the contrast and vice versa.

For each intensity frame in the time series we calculated the velocity map using the sLASCA method. This allowed following the aphids' activity (movements or internal flows) with the respective temporal resolution over long or short periods of time. However, for the sake of clarity, here, we present only the mean velocity map obtained by averaging of all single velocity maps, Fig. 5(b) and Fig. 5(e). The map indicates the average activity over the course of the experiment and the maximum of the activity was found in the central part of the aphid bodies.

Since the mean velocity maps cannot reveal the temporal evolution of the activity, we decided to calculate and present the temporal evolution of the spatial average of the velocity within the aphid body, Fig. 5(c) and Fig. 5(f). Each velocity time point is the mean of all velocities within a spatial window (comprising the aphid's body) of the N-th velocity frame. Thus, one can observe if there are spikes of activity with time. In the present case we observe some spikes indicating that from time to time some of the aphids' activity increases suddenly for short periods of time, Fig. 5(c). The three aphids have different velocity spikes. Velocity is different for the left aphid (black line), and almost the same for the other two. The meaning of the velocity here depends on the activity that causes the observed speckle changes. Note that at this stage of the development of the technique, we cannot attribute the velocity pattern to distinct aphid activities like feeding,

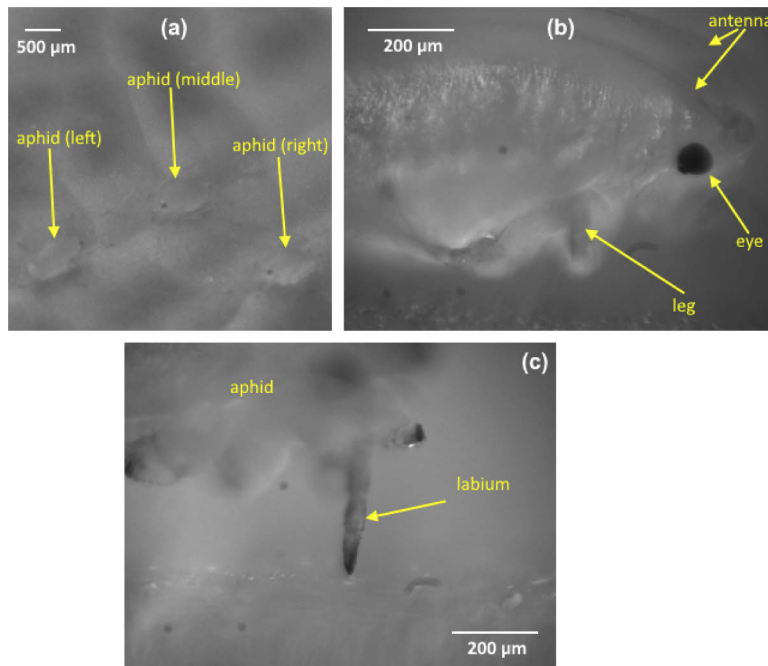


Fig. 4. White light illumination images of the aphids used in the LSCI experiments. (a) A group of three aphids (yellow arrows) feeding on a leaf for observing the feeding behavior with TL as camera objective to achieve wide FOV; (b) A single aphid feeding on a leaf – observing the feeding and after-feeding behavior with high resolution LSCI microscopy; (c) An aphid feeding through an artificial parafilm membrane. The labium touches the top side of the membrane and the stylets puncture it to access the feeding solution. Note that the camera focus is on the labium, therefore the aphid's body looks defocused.

hemolymph flow etc. What we observe, is a baseline activity with a rather stable long term trend and some irregular bigger spikes. The big spikes can be attributed to external movement of the aphid's body since they are visible on the recorded image frames.

In the short time scale feeding, Fig. 5(f), there are slight differences in the activity depending on the aphid observed. In the present case we see fast changing short spikes and a slower periodic pattern. The latter shows that the velocity or the activity fluctuates periodically around a mean value with a period of roughly 0.5 s. This slower periodic pattern might show a pressure wave resulting from heart beats or circulatory hemolymph flows causing the body of the aphid to contract.

The short time scale velocity is higher than the baseline velocity in the long time scale measurement (compare Fig. 5(c) and Fig. 5(f)). This is due to the approximation used for the calculation of the decorrelation time, i.e. $\tau_c = TK^2$ (Eq. (5)). However, in the reality the relationship is more complex, Eqs. (3) or (4), and since it is not possible to find analytical expression for $\tau_c(K, T)$ one either must solve $K(T, \tau_c)$ for τ_c numerically or use an approximation (which we did). This means that for the given acquisition settings, i.e. used exposure times, the changes in the contrast are too small to evaluate them properly (and thus calculate the proper velocity). For this, one needs to use the complete relation $K(T, \tau_c)$ as well as have negligible noise. For exposures $T < 2\tau_c$ the changes in the contrast are small, and they might be easily buried in noise. Thus, optimal acquisition conditions require an exposure time T at least two or more times longer than the correlation time τ_c . Therefore, we consider only the relative changes, which shows the type of the dynamics.

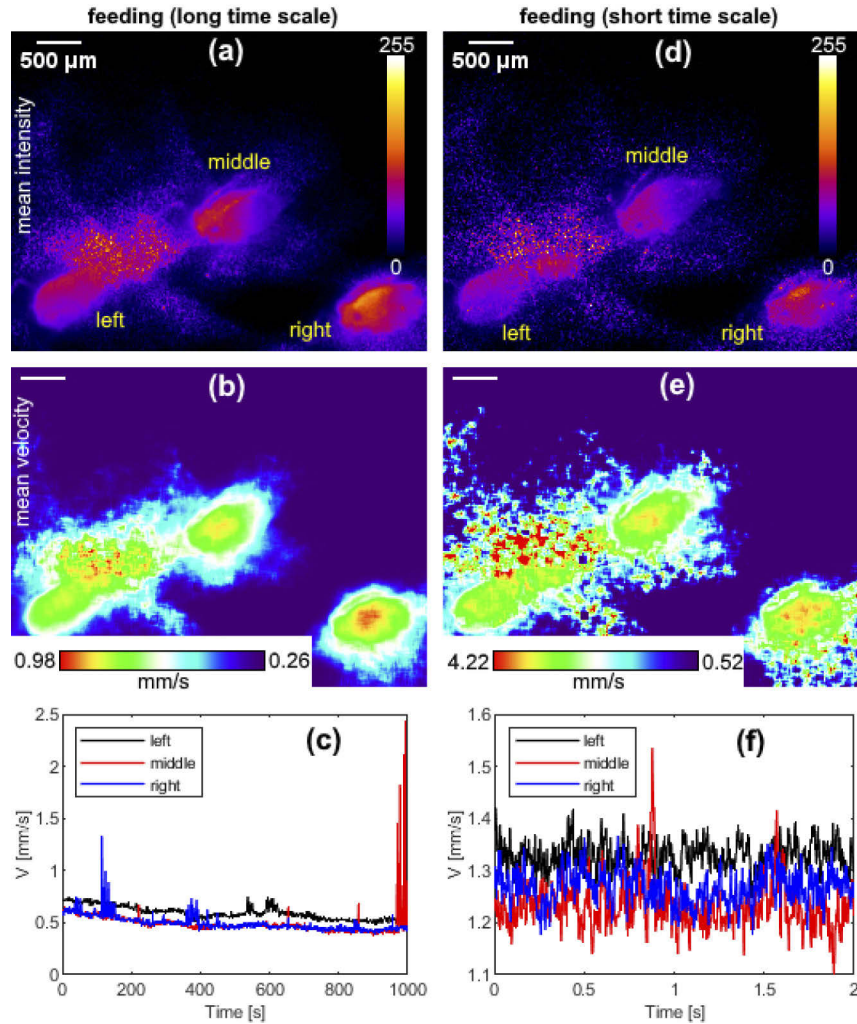


Fig. 5. Observing the feeding behavior of a group of aphids on a leaf by LSCI (0.4x magnification, NA = 0.1). The first column represents long time scale feeding (monitoring for 1000 s, 1 fps, 4 ms exposure time), the second column short time scale feeding (monitoring for 2 s, 500 fps, 2 ms exposure time). First row, (a) and (d), shows the mean intensity in time of the accumulated 2D images in the time series taken for each experiment. Second row, (b) and (e), is the mean velocity map (time average of all single velocity maps in the series) of the aphids calculated using the sLASCA algorithm (5×5 pixel window). The color bars indicate the range between the minimum and maximum velocity in units of mm/s. The scale bar for all images is 500 μm . Third row, (c) and (f), is the evolution in time of the velocity averaged within a spatial window comprising the entire body of each aphid.

3.2. Single aphid feeding on a leaf – feeding and after-feeding experiments with high resolution LSCI

In the next series of experiments, we imaged a single aphid in higher resolution LSCI mode with 10x/0.28NA Mitutoyo objective, Fig. 4(b). We compared the activity of a single aphid while feeding on a leaf, Fig. 6, with the same aphid while not feeding (Fig. 7). The non-feeding aphid (here called after-feeding) was immobilized on a double-faced scotch tape after the end of the feeding. While such immobilization can eventually affect the natural behavior of the aphid it allows to use high resolution LSCI to probe the aphid's activity locally, i.e. obtaining the distribution map of the activity across the whole body (no tracer particles were used). A video of the feeding is available (see [Visualization 2](#)) showing the corresponding laser speckle pattern dynamically changing due to the internal body activity.

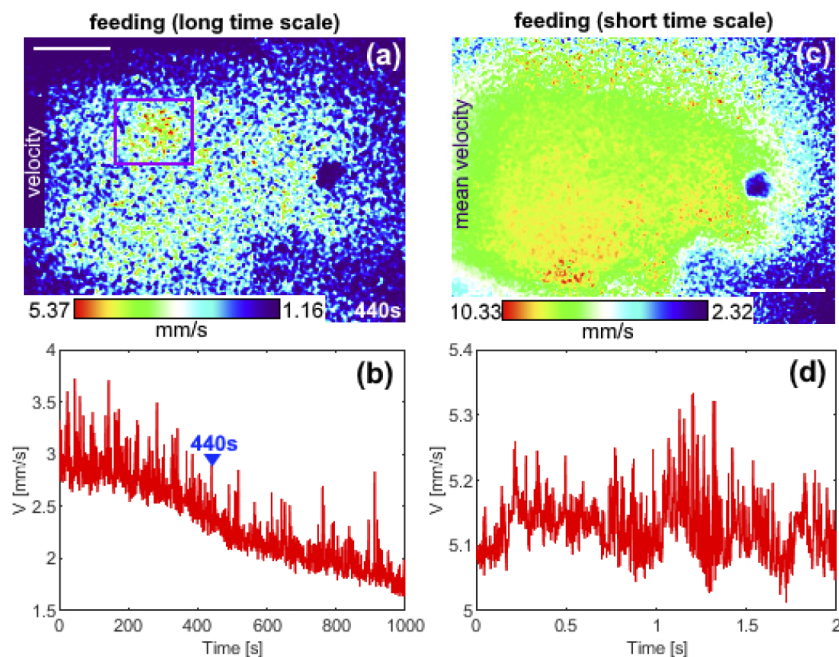


Fig. 6. Observing the feeding behavior of an aphid on a leaf by LSCI (5x magnification, NA = 0.28, illumination with 633 nm laser). The first column shows long time scale feeding (1000 s, 1 fps, 4 ms exposure time), (a) only shows the spatial velocity map calculated by sLASCA (7×7 pixel window) using a single frame taken at the 440th second [see also the peak marked with the blue triangle on (b)], while (b) is the time evolution of the spatial average of the velocity within the ROI (the violet rectangle); the second column shows the short time scale feeding (2 s, 500 fps, 2 ms exposure time), (c) presents the time average of all calculated velocity frames in the time series (each frame calculated by sLASCA, 5×5 pixel window), while (d) is the time evolution of the spatial average of the velocity within the entire aphid. Thus, one can monitor the activity within a given ROI or the entire area. The color bars indicate the range between the minimum and maximum velocity in units of mm/s. The scale bar for all images is 200 μ m.

The distribution of activity of a single aphid feeding on a leaf is shown on Fig. 6(a). Within the aphid we could identify a Region of Interest (ROI), outlined in violet color, where some increase in the activity occurred. This turned out to be a periodic beating pattern, which we monitored by observing the spatial average of the velocity within the given ROI, Fig. 6(b). The presented velocity map in Fig. 6(a) was observed at the 440th second. It seems that this pattern

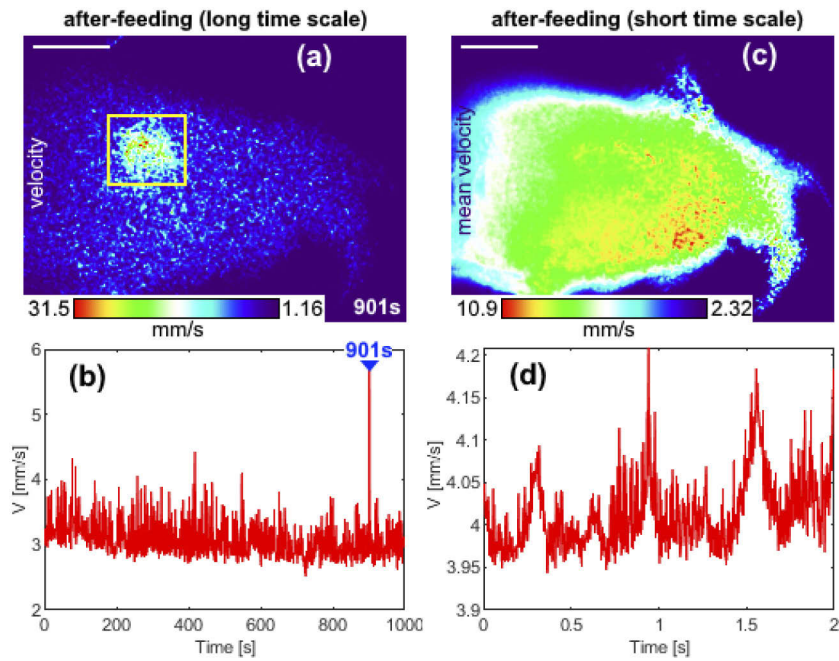


Fig. 7. Observing the after-feeding behavior of the same aphid, as in the previous figure, by LSCI (5x magnification, NA = 0.28, illumination with 633 nm laser). First column represents long time scale after-feeding (monitoring for 1000 s, 1 fps, 4 ms exposure time), (a) only shows the spatial velocity map calculated by sLASCA (5×5 pixel window) using a single frame taken at the 901st second [see also the peak marked with the blue triangle on (b)], while (b) is the time evolution of the spatial average of the velocity within the ROI (the yellow rectangle); the second column shows the short time scale feeding (2 s, 500 fps, 2 ms exposure time), (c) presents the time average of all calculated velocity frames in the time series (each frame calculated by sLASCA, 5×5 pixel window), while (d) is the time evolution of the spatial average of the velocity within the entire aphid. Thus, one can monitor the activity within a given ROI or the entire area. The color bars indicate the range between the minimum and maximum velocity in units of mm/s. The scale bar for all images is 200 μ m.

with varying amplitude and frequency (ca. 0.05 Hz) appears throughout the entire measurement. Such pattern would not be possible to observe without using LSCI microscopy, since there are no visible movements on the surface of the insect. Note that the steady decrease of the velocity with time in Fig. 6(b) is due to slight changes in the illumination intensity – this can influence the static scattering and in turn the base of the curve, however the activity patterns (peak shapes) are not affected.

The respective short time scale (2 sec, high temporal resolution) feeding activity map, Fig. 6(c), shows the resulting spatial distribution of the velocity, which is the average of all velocity frames in the given period. The temporal evolution of the activity per frame (i.e. the average velocity per frame) is shown in Fig. 6(d). We can see that there are slower frequency variations superimposed with higher frequency pattern with peaks. For the time being we cannot attribute this pattern to a specific source – it requires further investigation in the future.

Next, we removed the aphid from the leaf and immobilized it on a scotch tape so that we can observe its activity after the feeding ended (Fig. 7). It can be seen again, Fig. 7(a), that there is a ROI (yellow rectangle) where the activity increased sharply. The ROI coincides with

the ROI from the feeding activity mapping, Fig. 6(a), which means that the underlying process is not related to aphid feeding activity. The strongest beat occurred at 901st second and the overall beating time evolution (within the yellow rectangle) is shown on Fig. 7(b). The pattern appears periodically with varying amplitude and frequency (ca. 0.1 Hz), but the highest peak was recorded at the 901st second. Such pattern might be due to heart beat because (a) it is near the dorsal location where the heart is normally located, and (b) it is present in feeding and after-feeding, i.e. it is not related to feeding. The full activity patterns as well as the beating can be seen in the [Visualization 3](#).

The respective short time scale after-feeding activity is shown in Fig. 7(c)–7(d). One can visualize the spatial distribution of the activity during the whole acquisition, Fig. 7(c). The temporal evolution of the activity per frame, i.e. the average velocity within the aphid body per frame, is shown in Fig. 7(d). We can see that there are some slow variations in the activity superimposed with series of fast and discrete peaks. These slow variations can be interpreted as pronounced internal contractions of the aphid, which might be due to the circulatory hemolymph system, but for the time being the true physical origin is unknown.

Overall, we identified an interesting activity (hidden beating of unknown origin) and monitored its time evolution. The differences between feeding and non-feeding behavior are rather small, but they do exist. The data shows that the aphid is more still during feeding – visible by a smaller number of abrupt events and lower amplitude in the slow frequency variations.

3.3. Single aphid feeding on a parafilm membrane sachet – measuring flow in the stylets of an aphid

A good method for *in vivo* measurement of the flow rate or velocity inside aphid stylets is still missing. Therefore, we conducted a series of LSCI measurements in order to get a first estimate of the flow velocity in the stylets, *in vivo*, by feeding an aphid on an artificial parafilm membrane with a sucrose solution containing tracer particles, Fig. 4(c). LSCI is promising for this purpose as it can probe deep in the tissue. However, since the application of this method to aphids is not yet fully developed, the results here should be regarded as preliminary. Note that LSCI can give information about the type of the underlying process as well. For example, statistical random processes (e.g. diffusion, flow etc.) will render the observed auto-covariance curve exponentially decaying, while a periodic process (e.g. vibrations) will introduce periodicity in the curve. Estimating the flow velocity in the stylets can be valuable to better understand the different feeding activities (phloem feeding, xylem drinking, salivation, egestion) of aphids and their interaction with plants. It could also give an idea about the mechanical pressure or stress exercised on plant viruses that bind for transmission to the inner surface of the stylets. This can be helpful to identify or characterize the eventual contribution of hydrodynamic forces on the detachment conditions of such viruses (e.g. CaMV – Cauliflower Mosaic Virus [27]).

We used an artificial feeding solution (10% sucrose in water) to which we added tracers in order to obtain sufficient light scattering. As tracers we used 100 nm diameter PS nanoparticles which are still small enough so that they can freely pass through the stylet – note that the stylet cross-section has a diameter of ca. 300-500 nm at their narrowest part. The final concentration of the PS nanoparticles in the artificial feeding solution was 5 mg/mL (5x dilution from the stock solution). High enough concentration is needed to ensure the stochastic nature of the auto-covariance curve. Its exponentially decaying behavior is due to light scattering of high number of indistinguishable particles, i.e. the signal is a result of the ensemble average behavior. It is also important to ensure that no cross-correlation is observed between different spatial points since theory is only valid for such conditions.

The results from LSCI flow measurements (*in vivo*) in aphid stylets are shown in Fig. 8. Fig. 8(a) shows the mean intensity map (averaging over all frames in the time series), while Fig. 8(b) presents the Intensity vs time curve for a single pixel in the center of region 1. In order

to capture eventual fast flow velocities, we recorded the laser speckle with the highest possible camera frame rate, i.e. 500 fps and 2 ms exposure time. These parameters were chosen such that one could produce any exposure (e.g. multi-exposure frames) that is multiple of 2 ms. This allows to apply sMESI or FDLSI methods on the raw LSCI speckle data in order to estimate the flow velocity by fitting the respective contrast or auto-covariance curves with a model, Fig. 8(c) and Fig. 8(d). We selected three central regions from the labium, see the yellow rectangles in Fig. 8(a), beneath which the stylets should be located (Fig. 3) and that are therefore suitable for measurements.

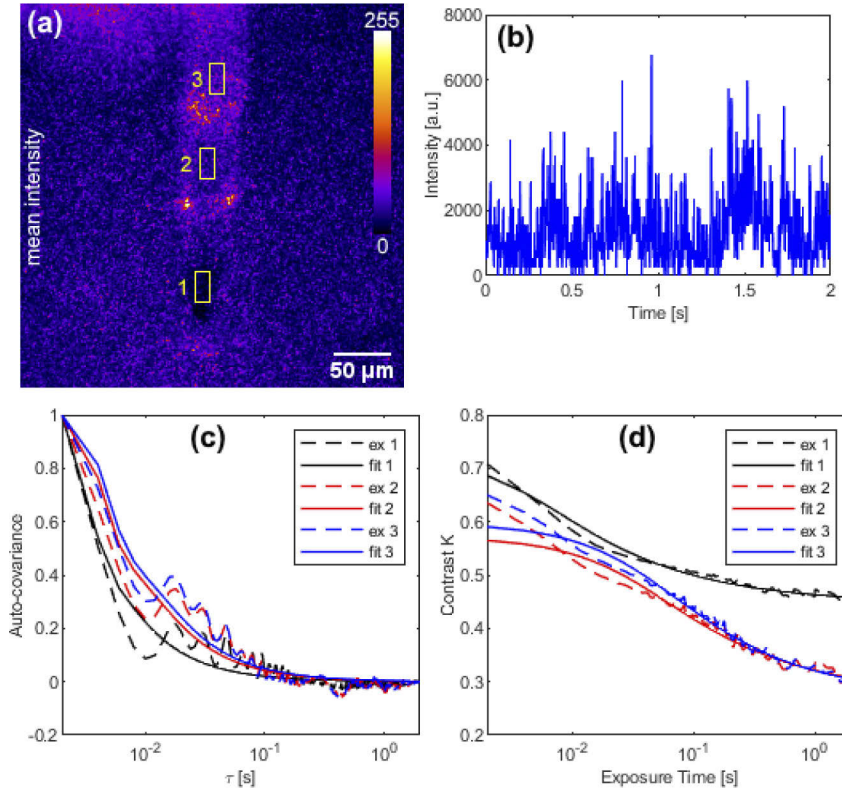


Fig. 8. Measuring the flow velocity in the stylets of an aphid by LSCI microscopy (5x magnification, NA = 0.28, illumination with 633 nm laser light). We used 2 s acquisition time, 500 fps and 2 ms exposure time for the camera settings. The mean intensity map is shown in (a) with the three regions (yellow rectangles) used for estimation of the flow velocity. (b) shows the time trace of the intensity of one pixel in the center of region 1. Note that each region contains 10×20 pixels. The average auto-covariance from each region is plotted in (c), while the average contrast K is plotted in (d). The designation “ex” stands for the experimental raw data and “fit” for the fitted curves, respectively. From the fitting of the auto-covariance we estimated the flow velocity to be in the range of 0.27 mm/s (region 1, black curves), 0.18 mm/s (region 2, red curves) and 0.15 mm/s (region 3, blue curves). On the other side, fitting the contrast K vs Exposure time curves by the sMESI method, yielded 0.26 mm/s (region 1, black curves), 0.035 mm/s (region 2, red curves) and 0.033 mm/s (region 3, blue curves). The last two values are not reliable as the fits did not converge well (compare dashed lines with continuous lines).

In Fig. 8(c), we plotted the average auto-covariance from each region resulting by averaging 10×20 auto-covariance curves. This allowed us to use the FDLSI method and to fit the auto-covariance $C_r(\tau)$ directly and extract the flow velocity, which is a fit parameter. The fit model for the FDLSI flow velocity assumes that the velocity distribution is known and follows unordered (Brownian) and ordered (highly directed) motion (Eq. (8)). This model gave a better fit than the initially chosen single speed flow velocity model (Eq. (7)). This can be likely explained with the noise in the data due to vibrations in the setup or in the sample, induced from the environment, which generated ripples distorting the curves – see the raw experimental data marked with “ex” in Fig. 8(c). Additionally, such fit, as taken here, would account for the influence of the diffusion on the extracted flow velocity – slow flow velocity would make the contribution of the Brownian motion more visible in the curve. The velocity obtained from the fits in the three regions was found to be between 0.15–0.27 mm/s. This difference in the values can be explained by the fact that the diameter of the food canal in the stylets varies along its length; it is narrower at the tip of the labium (hence the highest velocity is detected there) and wider at the head of the aphid.

As a next step we analyzed the data by using sMESI method, Fig. 8(d), and compared the resulting flow velocities with those obtained with FDLSI. In theory both methods are equivalent, but fitting $K(T)$ gives more flexibility as the frame rate is not a limit, and thus, can catch much faster processes. It has other advantages as well – for example, it accounts for the static scattering, experimental noise and acquisition geometry. This in turn gives more precise and quantitative flow estimations. Note that K for each exposure time T on the graph is calculated in a more elaborated way – from all the acquired single exposure frames in the time series we calculated the respective synthetic multi-exposure intensity frames in the post processing by binning the raw frames in time. For example, for each synthetic exposure time (e.g. $2T, 3T, 4T, \dots$) we produced a series of all possible frames with the given exposure. Then we used these frames to calculate (by stLASCA) single K value for the entire volume – in XY this is the ROI and in Z it is the number of the synthetic frames with given synthetic exposure time. Performing this procedure for all synthetic exposures allowed to produce the $K(T)$ curve.

Note that, from the curve $K(T)$, one can in theory recover the auto-covariance $C_r(\tau)$ curve (see Eq. (S19)). However, to obtain such a curve, high-quality data (very good statistics and minimal noise) is needed because the second derivative in Eq. (S19) is very sensitive to fluctuations in the data. Thus, we simply used the MESI fit model for $K(T)$ curve to estimate the correlation time τ_c (Eq. (4)) and in turn the flow velocity by the single velocity model (Eq. (9)). This model was derived assuming Lorentzian distributions of velocities, i.e. the auto-correlation function was $g_1(\tau) = \exp(-\tau/\tau_c)$. In our case, the fit gave the following flow velocities, Fig. 8(d): 0.26 mm/s (black curves), 0.035 mm/s (red curves) and 0.033 mm/s (blue curves). The fit of the black dashed K curve gave a result (0.26 mm/s), which is very similar to what we obtained with the FDLSI analysis. With respect to the other $K(T)$ curves the fit did not converge well due to other processes present which the fit equation could not account for. The other processes were most likely related to vibrations in the system as the FDLSI analysis indicates, Fig. 8(c).

Note that the LSCI method measures the flow speed in terms of length/time. In the case where the flow rate (volume/time) is of interest, one needs to determine in addition the diameter of the cross-section of the stylets (i.e. the food canal contained) where the velocity was measured and integrate the flow velocity over it. We did not do this here because of lack of an appropriate method to measure the stylet cross-section. However, as an approximation one could use data reported in the literature, obtained by microscopy on dissected stylets from different aphid species (for example book chapter: [28]). Thus, if we assume 1 μm stylet diameter and 0.2 mm/s flow speed we obtain flow rate of ca. 0.12 pL/s.

It is important to note that LSCI, in principle, cannot distinguish the flow direction. This means that by analyzing the speckle it is not possible to distinguish between in- and out-flow, i.e. if the flow is going inside the stylets or outside. However, if the flow speed in one direction

is much different than in the other (which we do not know), one could use it as a criterion to determine if the aphid is sucking or expelling liquid.

4. Discussion and outlook

LSCI microscopy can easily extract and detect spikes of activity, externally as well as internally, see for example Fig. 7. However, it cannot identify the cause of the observed speckle. For this, additional experiments are necessary, for example, doing measurements on anesthetized aphids or on different body parts to understand the origin of the speckle, i.e. if it is due to internal (hemolymph or food/saliva) flows, internal muscle contractions or external motion. The latter is relatively easy to recognize because it is visible. Alternatively, using other complementary techniques can be helpful (see below).

Care must be taken to ensure sufficient statistics in LSCI experiments. One way to improve the experimental and processing methodology is to optimize the choice of acquisition time, fps, exposure time and the pixel-to-speckle ratio. For example, one can extend the long time scale LSCI from 1000 sec to 10 000 sec and/or extend the short time scale experiment to 10-100 sec. Regarding the experiments with aphids – to capture all major activities, the best is to observe for hours and continuously. This might be helpful to catch transitions between the different feeding modes, i.e. how pre-feeding, feeding and after-feeding behavior shows up in the LSCI data.

A great advance would be combining LSCI with EPG measurements as this can help to correlate flow (or movement) with distinct aphid behaviors (running, probing, salivating, phloem feeding, xylem drinking etc.) and increase our knowledge of the different phases of the feeding process. Also new insight in transmission of stylet-retained plant viruses would be possible. Other interesting new experiments can be to observe aphid growth activity and growth rate as well as aphid low temperature dynamics to evaluate background due to non-biological processes such as diffusion. Furthermore, the LSCI technique is not limited to aphids, but can be applied to other insects: mosquitos, drosophila, whiteflies, etc. In this respect, we present here a first “proof of concept” study.

Although we provide here some evidence of hemolymph flow in living aphids, the proportion of static scattered and absorbed light from the chosen illumination wavelength (633 nm) was rather high to allow for proper visualization of the underlying cardiovascular system or a related structure. There is a potential for improvement by using longer illumination wavelength so that the light penetrates deeper in the body of the aphid and the internal structures become visible in LSCI. Also, one can play with the type of illumination; widefield illumination to study an entire aphid or spatially shaped laser light illumination [29,30] to localize the origin of speckle dynamics and increasing the depth resolving capabilities. The same applies to observation of food flows in the stylets, although there we obtained more quantitative results.

Further refinement of LSCI setup, methodology and experiments are possible. For example, reducing or correcting for vibrations, using SPDs (single photon detectors) to filter by photon path lengths (like in the time of flight approach), focusing the illumination beam on the stylets for flow rate experiments, using the photothermal effect to enhance detection of buried structures with LSCI [31], applying PCA (principle component analysis) to LSCI data to exclude static scattering and enhance its depth resolving abilities [32]. Adding a second camera channel to record simultaneously the horizontal and vertical polarization or different wavelengths or different magnifications (big/small areas). SERS (Surface Enhanced Raman Scattering) nanoparticles can be used as probes to obtain additional information like the pH or redox state in the stylet fluids (ingested and egested food, saliva) or in the hemolymph, *in vivo*. The optics can be improved by using even higher NA objectives - this would facilitate further the observation of flows in the stylets and increase the resolution of the 2D activity maps.

Other more complex techniques, related to or complementary to LSCI, can be helpful in the future to address problems with high tissue scattering and visualizing deeper aphid structures:

(1) deep tissue measurements of flow with SCOS (speckle contrast optical spectroscopy) [33], (2) path length resolved DCS (diffusion correlation spectroscopy) for depth resolved sensing [34], (3) non-contact laser induced ultrasound for imaging structures underneath the surface [35], (4) ballistic imaging with optical time gating to image different depths and reconstruct a 3D image of the object [36], (5) heterodyning techniques with a frequency modulated diode laser [37], (6) Doppler optical cardiogram gated 2D color flow imaging [38], DCS or iDWS (interferometric diffusion wave spectroscopy) for deeper tissue observation [12,13].

5. Conclusion

We demonstrated here as a proof of concept that LSCI microscopy can be used to monitor the activity of aphids remotely, i.e. without touching or disturbing the insect. External movements as well as internal activities (flows and muscles) can be monitored. Every process, which causes a change in the scattered photon path lengths, leads to changes in the observed speckle pattern and thus can be monitored by LSCI.

We conducted a few different preliminary experiments and present the respective analyses that can be done. Identifying interesting events and following their evolution was possible. For example, we present evidence of periodic activity in the dorsal region of the aphid body that might be attributed to heart beat or other muscular activity. In addition, we observed flow in the stylet region that is probably correlated with food flow and performed a quantitative estimation of the velocity (ca. 0.15–0.27 mm/s). However, further experiments are required to optimize conditions for recording (wavelength, illumination, optics) and analysis (model and statistics). Complementary experiments are required to identify the true origin of the recorded activities.

Overall, LSCI is a simpler and economical alternative to DCS or DLS, plus it can observe in 2D and thus obtain the two-dimensional activity map. A basic experimental setup only consists of a coherent light source (e.g. laser), an objective and a camera. Postprocessing is relatively fast and straightforward.

Funding. Human Frontier Science Program (RGP0013/2015).

Acknowledgments. We thank Claire Villeroy (INRAE Colmar) for aphid raising.

Disclosures. The authors declare no conflict of interest.

Data availability. The raw data underlying the results presented in this paper are not publicly available at this time but may be obtained from the authors upon reasonable request.

Supplemental document. See [Supplement 1](#) for supporting content.

References

1. S. Dinant, J.-L. Bonnemain, C. Girousse, and J. Kehr, "Phloem sap intricacy and interplay with aphid feeding," *C. R. Biol.* **333**(6-7), 504–515 (2010).
2. E. Prado and W. F. Tjallingii, "Aphid activities during sieve element punctures," *Entomologia Experimentalis et Applicata* **72**, 157–165 (1994).
3. W. F. Tjallingii and T. H. Esch, "Fine structure of aphid stylet routes in plant tissues in correlation with EPG signals," *Physiol. Entomol.* **18**(3), 317–328 (1993).
4. V. Nalam, J. Louis, and J. Shah, "Plant defense against aphids, the pest extraordinaire," *Plant Sci.* **279**, 96–107 (2019).
5. W. F. Tjallingii, "Regulation of Phloem Sap Feeding by Aphids," in *Regulatory Mechanisms in Insect Feeding*, R. F. Chapman and G. de Boer, eds. (Springer, US, 1995), pp. 190–209.
6. W.-K. Lee and J. J. Socha, "Direct visualization of hemolymph flow in the heart of a grasshopper (*Schistocerca americana*)," *BMC Phys.* **9**(1), 2 (2009).
7. R. T. V. Chintapalli and J. F. Hillyer, "Hemolymph circulation in insect flight appendages: physiology of the wing heart and circulatory flow in the wings of the mosquito *Anopheles gambiae*," *J. Exp. Biol.* **219**(Pt 24), 3945–3951 (2016).
8. A. F. Fercher and J. D. Briers, "Flow visualization by means of single-exposure speckle photography," *Opt. Commun.* **37**(5), 326–330 (1981).
9. D. A. Boas and A. K. Dunn, "Laser speckle contrast imaging in biomedical optics," *J. Biomed. Opt.* **15**(1), 011109 (2010).

10. D. Briers, D. D. Duncan, E. Hirst, S. J. Kirkpatrick, M. Larsson, W. Steenbergen, T. Stromberg, and O. B. Thompson, "Laser speckle contrast imaging: theoretical and practical limitations," *J. Biomed. Opt.* **18**(6), 066018 (2013).
11. J. Senarathna, A. Rege, N. Li, and N. V. Thakor, "Laser Speckle Contrast Imaging: Theory, Instrumentation and Applications," *IEEE Rev. Biomed. Eng.* **6**, 99–110 (2013).
12. D. J. Pine, D. A. Weitz, P. M. Chaikin, and E. Herbolzheimer, "Diffusing wave spectroscopy," *Phys. Rev. Lett.* **60**(12), 1134–1137 (1988).
13. W. Zhou, O. Kholidov, S. P. Chong, and V. J. Srinivasan, "Highly parallel, interferometric diffusing wave spectroscopy for monitoring cerebral blood flow dynamics," *Optica* **5**(5), 518 (2018).
14. P. Li, S. Ni, L. Zhang, S. Zeng, and Q. Luo, "Imaging cerebral blood flow through the intact rat skull with temporal laser speckle imaging," *Opt. Lett.* **31**(12), 1824 (2006).
15. P. Zakharov, A. C. Völker, M. T. Wyss, F. Haiss, N. Calcinaghi, C. Zunzunegui, A. Buck, F. Scheffold, and B. Weber, "Dynamic laser speckle imaging of cerebral blood flow," *Opt. Express* **17**(16), 13904 (2009).
16. H. Cheng, Y. Yan, and T. Q. Duong, "Temporal statistical analysis of laser speckle images and its application to retinal blood-flow imaging," *Opt. Express* **16**(14), 10214 (2008).
17. T. F. Döring, "How aphids find their host plants, and how they don't: Aphid host finding," *Ann Appl. Biol.* **165**, 3–26 (2014).
18. R. Bandyopadhyay, A. S. Gittings, S. S. Suh, P. K. Dixon, and D. J. Durian, "Speckle-visibility spectroscopy: A tool to study time-varying dynamics," *Rev. Sci. Instrum.* **76**(9), 093110 (2005).
19. S. M. S. Kazmi, E. Faraji, M. A. Davis, Y.-Y. Huang, X. J. Zhang, and A. K. Dunn, "Flux or speed? Examining speckle contrast imaging of vascular flows," *Biomed. Opt. Express* **6**(7), 2588 (2015).
20. M. A. Davis, L. Gagnon, D. A. Boas, and A. K. Dunn, "Sensitivity of laser speckle contrast imaging to flow perturbations in the cortex," *Biomed. Opt. Express* **7**(3), 759 (2016).
21. J. C. Ramirez-San-Juan, R. Ramos-Garcia, G. Martinez-Niconoff, and B. Choi, "Simple correction factor for laser speckle imaging of flow dynamics," *Opt. Lett.* **39**(3), 678 (2014).
22. A. Nadort, R. G. Woolthuis, T. G. van Leeuwen, and D. J. Faber, "Quantitative laser speckle flowmetry of the in vivo microcirculation using sidestream dark field microscopy," *Biomed. Opt. Express* **4**(11), 2347 (2013).
23. J. C. Ramirez-San-Juan, R. Ramos-García, I. Guizar-Iturbide, G. Martínez-Niconoff, and B. Choi, "Impact of velocity distribution assumption on simplified laser speckle imaging equation," *Opt. Express* **16**(5), 3197 (2008).
24. H. Li, Q. Liu, H. Lu, Y. Li, H. F. Zhang, and S. Tong, "Directly measuring absolute flow speed by frequency-domain laser speckle imaging," *Opt. Express* **22**(17), 21079 (2014).
25. A. B. Parthasarathy, W. J. Tom, A. Gopal, X. Zhang, and A. K. Dunn, "Robust flow measurement with multi-exposure speckle imaging," *Opt. Express* **16**(3), 1975 (2008).
26. LSCI - Laser Speckle Contrast Imaging Toolbox, <https://github.com/stoyan-yordanov/LSCI> (2021).
27. C. G. Webster, E. Pichon, M. van Munster, B. Monsion, M. Deshoux, D. Gargani, F. Calevro, J. Jimenez, A. Moreno, B. Krenz, J. R. Thompson, K. L. Perry, A. Fereres, S. Blanc, and M. Uzest, "Identification of Plant Virus Receptor Candidates in the Styles of Their Aphid Vectors," *J. Virol.* **92**(14), e00432 (2018).
28. A. R. Forbes, "THE MOUTHPARTS AND FEEDING MECHANISM OF APHIDS," in *Aphids As Virus Vectors* (Elsevier, 1977), pp. 83–103.
29. A. Mazhar, D. J. Cuccia, T. B. Rice, S. A. Carp, A. J. Durkin, D. A. Boas, B. Choi, and B. J. Tromberg, "Laser speckle imaging in the spatial frequency domain," *Biomed. Opt. Express* **2**(6), 1553 (2011).
30. E. Du, S. Shen, S. P. Chong, and N. Chen, "Multifunctional laser speckle imaging," *Biomed. Opt. Express* **11**(4), 2007 (2020).
31. C. Regan, J. C. Ramirez-San-Juan, and B. Choi, "Photothermal laser speckle imaging," *Opt. Lett.* **39**(17), 5006 (2014).
32. J. A. Arias-Cruz, R. Chiu, H. Peregrina-Barreto, R. Ramos-Garcia, T. Spezzia-Mazzocco, and J. C. Ramirez-San-Juan, "Visualization of in vitro deep blood vessels using principal component analysis based laser speckle imaging," *Biomed. Opt. Express* **10**(4), 2020 (2019).
33. T. Dragojević, J. L. Hollmann, D. Tamborini, D. Portaluppi, M. Buttafava, J. P. Culver, F. Villa, and T. Durduran, "Compact, multi-exposure speckle contrast optical spectroscopy (SCOS) device for measuring deep tissue blood flow," *Biomed. Opt. Express* **9**(1), 322 (2018).
34. M. Pagliazzi, S. K. V. Sekar, L. Colombo, E. Martinenghi, J. Minnema, R. Erdmann, D. Contini, A. D. Mora, A. Torricelli, A. Pifferi, and T. Durduran, "Time domain diffuse correlation spectroscopy with a high coherence pulsed source: in vivo and phantom results," *Biomed. Opt. Express* **8**(11), 5311 (2017).
35. X. Zhang, J. R. Fincke, C. M. Wynn, M. R. Johnson, R. W. Haupt, and B. W. Anthony, "Full noncontact laser ultrasound: first human data," *Light: Sci. Appl.* **8**(1), 119 (2019).
36. L. Fieramonti, A. Bassi, E. A. Foglia, A. Pistocchi, C. D'Andrea, G. Valentini, R. Cubeddu, S. De Silvestri, G. Cerullo, and F. Cotelli, "Time-Gated Optical Projection Tomography Allows Visualization of Adult Zebrafish Internal Structures," *PLoS One* **7**(11), e50744 (2012).
37. Z. Guan, P. Lundin, and S. Svanberg, "Assessment of photon migration in scattering media using heterodyning techniques with a frequency modulated diode laser," *Opt. Express* **17**(18), 16291 (2009).
38. A. Mariampillai, B. A. Standish, N. R. Munce, C. Randall, G. Liu, J. Y. Jiang, A. E. Cable, I. A. Vitkin, and V. X. D. Yang, "Doppler optical cardiogram gated 2D color flow imaging at 1000 fps and 4D in vivo visualization of embryonic heart at 45 fps on a swept source OCT system," *Opt. Express* **15**(4), 1627 (2007).